IEEE Photonics Journal
An IEEE Photonics Society Publication

Open Access

Single Negative Metamaterial-Based Hollow-Core Bandgap Fiber With Multilayer Cladding

Volume 7, Number 6, December 2015

Md Jubayer Shawon
Ghafour Amouzad Mahdiraji
Md. Munir Hasan
Barmak Honarvar Shakibaei
Shee Yu Gang
Mahdy Rahman Chowdhury Mahdy
Faisal Rafiq Mahamd Adikan

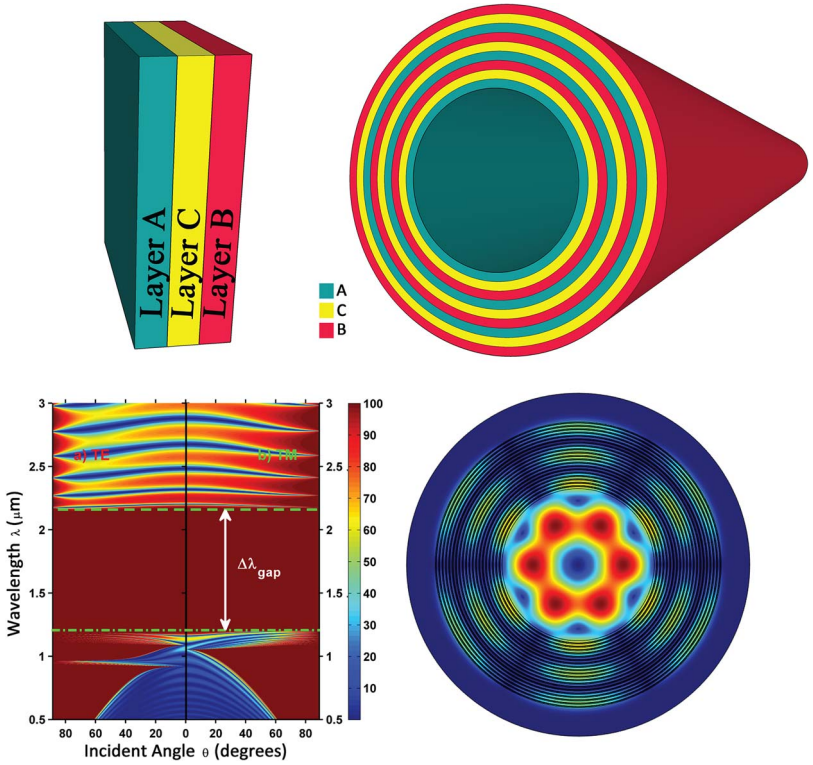

DOI: 10.1109/JPHOT.2015.2496399
1943-0655 © 2015 IEEE

IEEE photonics SOCIETY

IEEE

Single Negative Metamaterial-Based Hollow-Core Bandgap Fiber With Multilayer Cladding

Md Jubayer Shawon,[1] Ghafour Amouzad Mahdiraji,[1,4] Md. Munir Hasan,[2] Barmak Honarvar Shakibaei,[1] Shee Yu Gang,[1] Mahdy Rahman Chowdhury Mahdy,[3] and Faisal Rafiq Mahamd Adikan[1,4]

[1]Integrated Lightwave Research Group, Department of Electrical Engineering, Faculty of Engineering, University of Malaya, 50603 Kuala Lumpur, Malaysia
[2]Department of Electrical Engineering and Computer Science, The University of Tennessee, Knoxville, TN 37996 USA
[3]Department of Electrical and Computer Engineering, National University of Singapore, Singapore 117576
[4]Flexilicate Sdn. Bhd., University of Malaya, 50603 Kuala Lumpur, Malaysia

DOI: 10.1109/JPHOT.2015.2496399

Manuscript received August 24, 2015; revised October 19, 2015; accepted October 21, 2015. Date of publication October 29, 2015; date of current version November 25, 2015. This paper was supported by the University of Malaya High Impact Research under Grant UM.0000005/HIR.C1. Corresponding author: F. R. Mahamd Adikan (e-mail: rafiq@um.edu.my).

Abstract: We propose a single negative metamaterial (MTM)-based hollow-core fiber with multilayer cladding employing zero-effective-phase bandgap for optical confinement in this paper. The cladding is formed from a ternary 1-D photonic crystal (T-1DPC) unit cell, which is basically a Mu-negative material sandwiched by different Mu-negative and Epsilon-negative materials. We demonstrate its capability for broadband transmission by numerically simulating and analyzing the photonic bandgap (PBG) and the modal loss characteristics. The results show that the T-1DPC-based cladding can effectively broaden the PBG. Compared with that for the binary 1-D photonic crystal unit cell-based fiber, the radiation loss for the T-1DPC-based fiber can be reduced by three orders of magnitude over most of the PBG range for equal number of unit cells. This MTM fiber, depending on the operating wavelength, shows surface plasmon guidance or classical wave guidance or both simultaneously. We also investigate the effect of variations in the design parameters and material absorption on the wave guidance of this fiber.

Index Terms: Metamaterial, waveguide, surface plasmon, zero effective phase, cladding mode, Spatially Averaged Single Negative (SASN) bandgap.

1. Introduction

Metameterials (MTMs) are artificially engineered materials that show exotic electromagnetic properties, leading to many interesting phenomena and applications [1]–[8]. Waveguides are the most fundamental and important field of photonic research as it is the building block of all compact photonic devices and systems. Using the exceptional properties of MTMs, many interesting waveguides such as MTM-core fibers [9]–[14], MTM-cladding fibers [15], [16] have been investigated. They exhibit unusual guiding properties that traditional dielectric or metallic waveguides cannot produce. Slow and fast waves, synchronized forward and backward wave

propagation, backward waves, power circulation, and bifurcation are some of the interesting phenomena that MTM based waveguides show.

In the literature, hollow-core waveguides with hybrid cladding [17] and rolled-up metamaterials [18], [19] have also been studied. Moreover, large quantities of MTMs have recently been produced using fiber drawing technique that show Mu negative and epsilon negative material properties [20], [21]. This fiber drawing technique paves the way to realizing various MTM fiber structures that might have many novel applications.

By integrating the single negative (SNG) [22] MTM based photonic bandgap (PBG), it is theoretically possible to achieve reduced geometry cladding thickness for optical fibers. SNG materials are such that only one of the two material parameters is negative. These are epsilon negative (ENG) materials with $\epsilon < 0$ (but $\mu > 0$) or Mu negative (MNG) materials with $\mu < 0$ (but $\epsilon > 0$). By using two negative parameter materials like MNG-ENG in the form of multilayer periodic structure, a completely different kind of bandgap can be obtained called zero-effective-phase (ZEP) bandgap [23], [24]. This ZEP bandgap gives rise to another bandgap called Spatially Averaged Single Negative (SASN) bandgap [25], [26] under sub-wavelength condition $(k_i d_i \ll 1)$. Unlike Bragg gaps, these gaps originate from the interaction of evanescent waves in the MNG and ENG media [25], [27]. The fiber is similar to Bragg fiber in aspects such as guiding in air, polarization degeneracy, etc. Due to the localization of the field at the interfaces, ZEP gap is robust against disorder, independent on scaling and independent of incident angle and has same PBG for both TE and TM polarization [24], [25], [28]. Because SNG photonic crystal (PC) thickness does not need to be quarter wave thick like it does for Bragg PC at operating wavelength, it enables us to reduce the fiber size whereas for fibers with other PBGs this is not possible, which can lead to optical devices of very small size. Besides, by applying the concept of SASN bandgap, it is possible to control the band gap and its center frequency [25], [29], [30]. Such degrees of freedom are not found in conventional Bragg bandgaps that are employed in Bragg fibers to guide light.

Therefore, a Bragg-like fiber can be designed that employs MTM bandgap instead of Bragg bandgap as its guiding mechanism. This type of Bragg-like MTM based bandgap fiber has recently been studied on a binary-1-D photonic crystal (B-1DPC) unit cell system [31]. It showed excellent performance in terms of confinement loss and bandgap controlling. However, the problem of making the fiber broadband still remained. Furthermore, given the youth of such a topic, it is important to have a comprehensive study to address the effects of various design parameters on wave guidance. Here, we investigate ternary (T)-1DPC-based MTM fiber and its superiority over B-1DPC. The proposed fiber exhibits broadband transmission with low confinement loss. The bandgap designing of this type of fiber is also very straightforward as it utilizes one of the most flexible MTM bandgap called ZEP bandgap to confine light in the core. The fiber also shows combined surface plasmon and classical wave guidance phenomenon. The effect of material absorption properties on the total loss has also been studied.

2. Mathematical Background and Modeling

Experimental results show that Drude model can be used to describe the dispersion characteristics of fabricated SNG materials [32]–[34]. Numerous numerical simulations have also been carried out using Drude model [28], [35]–[37]. Therefore, in this work, we have employed the Drude model to describe the dispersion of our materials. According to the Drude theory [38], the dispersion of relative permittivity and permeability of the materials are given by

$$\epsilon_{MNG} = 1;\ \mu_{MNG} = 1 - \frac{\omega_{mp}^2}{\omega^2 + j\omega\gamma_m} \text{ for } MNG \tag{1}$$

$$\epsilon_{ENG} = 1 - \frac{\omega_{ep}^2}{\omega^2 + j\omega\gamma_e}\ ;\ \mu_{ENG} = 1 \text{ for } ENG. \tag{2}$$

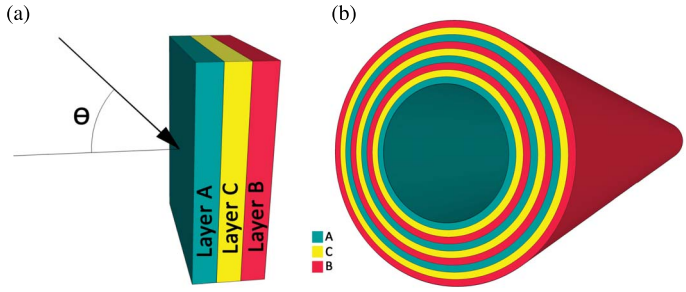

Fig. 1. (a) T-1DPC unit cell. (b) Hollow core fiber structure with SNG layers.

Here, ω_{mp} and ω_{ep} are magnetic plasma and electric plasma frequencies, respectively; γ_e and γ_m are corresponding electric and magnetic damping factors which account for the material loss.

The schematic diagram of the T-1DPC unit cell used in the proposed design is shown in Fig. 1(a). The proposed unit cell contains MNG material in layer *A* and ENG material in layer *B*. Furthermore, to make the bandgap broader [29], another layer of MNG material denoted as layer *C* is inserted between layer *A* and *B*. Then, a multilayer system in the form of $(ACB)^N$ is developed by cascading the unit cells *N* times. This multilayer system is then rolled up to form the proposed fiber as shown in Fig. 1(b).

Now, let us assume, the layers denoted by *A* (ϵ_A, μ_A), *B* (ϵ_B, μ_B), and *C* (ϵ_C, μ_C) have thickness of d_A, d_B, and d_C respectively. Here, $d = (d_A + d_B + d_C)$ is the period of one unit cell. For an infinite periodic structure $(N \to \infty)$ based on Bloch's condition, the dispersion relation for any incident angle θ follows the relation [39]

$$\begin{aligned}\cos(\kappa d) = &\cos(k_{Az}d_A)\cos(k_{Bz}d_B)\cos(k_{Cz}d_C)\\ &-\frac{1}{2}\left(\frac{q_{Az}}{q_{Bz}}+\frac{q_{Bz}}{q_{Az}}\right)\sin(k_{Az}d_A)\sin(k_{Bz}d_B)\cos(k_{Cz}d_C)\\ &-\frac{1}{2}\left(\frac{q_{Az}}{q_{Cz}}+\frac{q_{Cz}}{q_{Az}}\right)\sin(k_{Az}d_A)\cos(k_{Bz}d_B)\sin(k_{Cz}d_C)\\ &-\frac{1}{2}\left(\frac{q_{Bz}}{q_{Cz}}+\frac{q_{Cz}}{q_{Bz}}\right)\cos(k_{Az}d_A)\sin(k_{Bz}d_B)\sin(k_{Cz}d_C)\end{aligned} \tag{3}$$

where κ is the Bloch wave vector, and $k_{iz} = (\omega/c)\sqrt{\epsilon_i}\sqrt{\mu_i}\sqrt{1-\sin^2\theta/(\epsilon_i\mu_i)}$ is the component of wave vector along the axis of alternating layers in the *i*th medium (i.e., $i = A$, *B* or *C*). For TE wave, $q_{iz} = \sqrt{\epsilon_i}/\sqrt{\mu_i}\sqrt{1-\sin^2\theta/(\epsilon_i\mu_i)}$; for TM wave, $q_{iz} = \sqrt{\mu_i}/\sqrt{\epsilon_i}\sqrt{1-\sin^2\theta/(\epsilon_i\mu_i)}$, and *c* is speed of light in vacuum. In (3), when $\cos(\kappa d) > 1$, there is no real solution for κ which gives phase $\phi = \kappa d = 0$ and gives rise to ZEP band gap. Furthermore, if the sub-wavelength condition $(k_i d_i \ll 1)$ is satisfied, the conditions for the edges of the bandgap for the multilayer system can be written as [29]

$$\bar{\epsilon} = \sum_i \epsilon_i d_i = 0 \tag{4a}$$

$$\bar{\mu} = \sum_i \mu_i d_i = 0. \tag{4b}$$

It is obvious from (4a) and (4b) that the photonic bandgap control is quite straightforward. By changing the layer thicknesses or material dielectric parameters, it is possible to shift the band edges arbitrarily across the frequency spectrum.

In this work, we have used Transfer Matrix Method (TMM) to analyze the fiber. For longitudinal fields, the guided wave solution in the *i*th layer at radius *r* take the form of (5), shown below,

where A_i, B_i, C_i, and D_i are constants, and $\beta = \beta_r + j\beta_j$ is the propagation constant [40]. Since the wave vector is a complex number inside the SNG material, Bessel functions J and Y in the matrix $M_i(r)$, formulated in [41], have to be replaced with modified Bessel functions of first and second kind (I and K)

$$\begin{bmatrix} E_{zi} \\ \frac{1}{I\beta} H_{\theta i} \\ H_{zi} \\ -\frac{1}{I\beta} E_{\theta i} \end{bmatrix} = M_i(r) \begin{bmatrix} A_i \\ B_i \\ C_i \\ D_i \end{bmatrix} \tag{5}$$

where

$$M_i(r) = \begin{bmatrix} I_I(k_i' r) & K_I(k_i' r) & 0 & 0 \\ \frac{\omega\epsilon_i k_i'}{\beta k_i^2} I_I'(k_i' r) & \frac{\omega\epsilon_i k_i'}{\beta k_i^2} K_I'(k_i' r) & \frac{I}{k_i^2 r} I_I(k_i' r) & \frac{I}{k_i^2 r} K_I(k_i' r) \\ 0 & 0 & I_I(k_i' r) & K_I(k_i' r) \\ \frac{I}{k_i^2 r} I_I(k_i' r) & \frac{I}{k_i^2 r} K_I(k_i' r) & \frac{\omega\mu_i k_i'}{\beta k_i^2} I_I'(k_i' r) & \frac{\omega\mu_i k_i'}{\beta k_i^2} K_I'(k_i' r) \end{bmatrix}. \tag{6}$$

Here, $k_i' = \sqrt{|\omega^2\epsilon_i\mu_i + \beta_j^2 - \beta_r^2| - j\beta_r\beta_j}$, $k_i = \sqrt{\omega^2\epsilon_i\mu_i - \beta^2}$, and I is the azimuthal mode number. I and K are modified Bessel functions of first and second kind. Inside the core, I and K are replaced with regular Bessel functions J and Y, respectively. Hankel function is used for outermost cladding layer since there is no incoming wave generated by reflection from any other media. Imposing conditions of finite field in the core and zero inward traveling waves outside the fiber [42], we have calculated complex β.

The confinement loss (CL) in dB/km is calculated from the imaginary part of the propagation constant as $\text{CL} = (40\pi/\lambda \ln(10))\text{Im}(\beta c/\omega) \times 10^3$, where c is the speed of light in free space, and λ is the operating wavelength [42].

In this work, for layer A (MNG), $\omega_{mpA} = 1.73 \times 10^{15}$ Hz, and $d_A = 130$ nm; for layer B (ENG), $\omega_{epB} = 1.7889 \times 10^{15}$ Hz and $d_B = 50$ nm; and for the middle sandwiched layer C (MNG), $\omega_{mpC} = 2.0494 \times 10^{15}$ Hz and $d_C = 40$ nm has been chosen. With these parameters, we can achieve ZEP bandgap in the telecommunication region. It is important to recall that, ZEP bandgap is independent of scaling [24], [25], [28]. Hence, to make the fabrication of this fiber more feasible, the layer thicknesses chosen in this work can be scaled up without affecting the bandgap.

As mentioned before, to get ZEP bandgap, both types of SNG materials are required. Therefore, layer A (MNG) and B (ENG) are incorporated in the unit cell. Furthermore, a third material is required to be placed between layer A and B to make the fiber broadband. The choice of materials is either ENG or MNG. According to the method described in [29], we first proceeded with the $(AB)^N$ system. The upper band edge frequency comes at 1.47×10^{15} Hz which corresponds to $\overline{\mu} = 0$ condition, and the lower band edge frequency would be 9.43×10^{14} Hz that corresponds to $\overline{\epsilon} = 0$ condition. In this scenario, the third layer must be MNG to broaden the bandgap [29]. This is why, we have proposed $(ACB)^N$ system in which the layer C is comprised of MNG material.

Here, we have determined our PBG in the wavelength range where reflectivity is not less than 99% [43]. The normalized PBG width of $\Delta\lambda_n$ can be written as

$$\Delta\lambda_n = 2(\lambda_U - \lambda_L)/(\lambda_U + \lambda_L) \tag{7}$$

where λ_U and λ_L represent the upper and lower bandgap edge (UBGE and LBGE) wavelengths, respectively.

3. Results and Discussion

The T-1DPC-based MTM fiber differs from B-1DPC-based MTM fiber. To demonstrate its basic characteristics, firstly, the bandgap structure of the proposed $(ACB)^N$ (T-1DPC) is compared

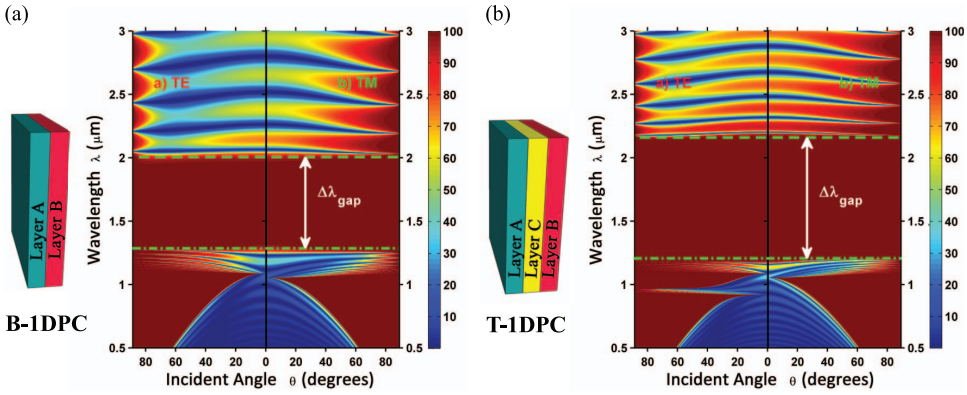

Fig. 2. Reflectivity spectra of B-1DPC (a) and T-1DPC (b) as a function of wavelength and incident angle for both TE and TM polarization. For T-1DPC: $d_A = 130$ nm, $d_C = 40$ nm, $d_B = 50$ nm, $\epsilon_A = 1$, $\mu_A = 1 - \omega_{mpA}^2/(\omega^2 + j\omega\gamma_{mA})$; $\epsilon_C = 1$, $\mu_C = 1 - \omega_{mpC}^2/(\omega^2 + j\omega\gamma_{mC})$; $\epsilon_B = 1 - \omega_{epB}^2/(\omega^2 + j\omega\gamma_{eB})$, and $\mu_B = 1$, where $\omega_{mpA} = 1.73 \times 10^{15}$ Hz, $\omega_{mpC} = 2.0494 \times 10^{15}$ Hz, and $\omega_{epB} = 1.7889 \times 10^{15}$ Hz. For B-1DPC, material A and B have exactly the same parameters as T-1DPC, except it does not have layer C. In both cases, $N = 15$.

with $(AB)^N$ (B-1DPC) system. The PBG, represented by the overlapped wavelength range in the omni-directional reflection spectra of TM and TE modes for $0^\circ < \theta^\circ < 89^\circ$ is shown in Fig. 2. These reflection spectra have been calculated using TMM. The bandgap generated by the multilayer cladding in this MTM based bandgap fiber, can be approximated to that of a planar multilayer structure [31], [43], [44]. In the following simulation, we set $N = 15$ and damping factor $\gamma_{mA} = \gamma_{mC} = \gamma_{eB} = 2\pi \times 10^3$ Hz. Other material parameters used in this simulation has been described earlier in the previous section. In our $(ACB)^N$ system, $\overline{\mu} = 0$ condition is satisfied at 1184 nm and $\overline{\epsilon} = 0$ condition is satisfied at 2210 nm. Theoretically, there should be a bandgap between these two wavelengths.

The wavelength ranges of the PBG are marked in Fig. 2 by the pairs of dotted lines. Fig. 2(a) shows, a ZEP bandgap that has been achieved in the B-1DPC structure between 1287 nm to 2010 nm wavelength with normalized PBG width of 0.4386. The ZEP bandgap for T-1DPC is in the 1196 nm to 2165 nm range, as shown in Fig. 2(b). As can be seen from Fig. 2, when $N = 15$, the normalized PBG width for the T-1DPC is 0.5766 which is significantly larger than the normalized width of 0.4386 for the B-1DPC.

A finite element (FE) simulation was also carried out using a commercial finite element solver (COMSOL) to justify the prediction. we have considered the same structure described in Fig. 2(b) for the FE analysis with 15 unit cells. We ensured at least 15 elements per wavelength across the simulation domain to find the mode profiles. The perfectly matched layer (PML) is implemented at outer boundary of the cladding to ensure zero reflection of the outgoing wave. Perfect confinement of HE_{11}, TM_{01} and TE_{01} modes at 1.55 μm can be observed from Fig. 3.

Although MNG and ENG layers are individually capable of supporting surface plasmons for TE and TM waves, respectively, the FE simulation results do not show any surface plasmons at 1.55 μm. This can be attributed to the fact that 1.55 μm is well within the ZEP bandgap region, and no wave leaks out of the core into the cladding. The FE simulation also shows that 99.98%, 99.89% and 99.93% of the modal power are contained within the core for HE_{11}, TE_{01}, and TM_{01} mode, respectively. It proves that the leakage to the cladding is very less.

It is important to recall that the bandgap in the proposed system ranges from 1196 nm to 2165 nm. At outside of this bandgap region, the cladding is no longer reflective. Therefore, the wave can leak out of the core, and the evanescent waves can trigger the surface plasmons in the cladding as shown in Fig. 3(d) and (e). Another interesting phenomenon occurs when the fiber is operating at outside of the bandgap region. FE analysis revealed that at outside of the

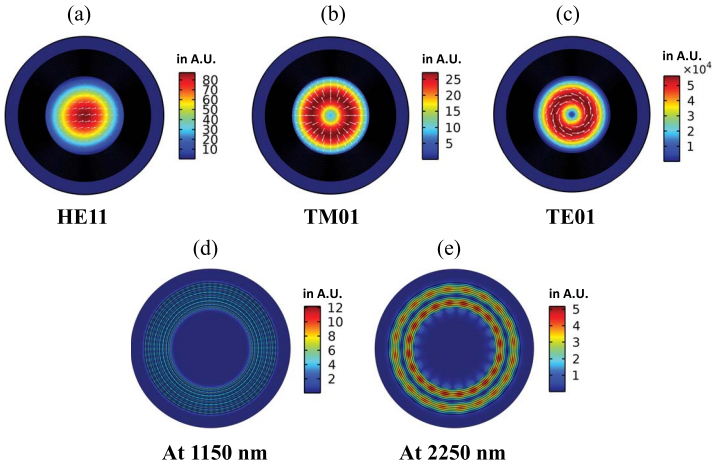

Fig. 3. Electric field distribution inside the core at $\lambda = 1.55$ μm (inside bandgap region) for different core modes from (a)—(c). (d) and (e) Electric field distribution of the surface plasmon modes at outside of the bandgap region. The real and imaginary part of the effective mode index of the mode shown in (d) are $\mathrm{Re}(n_{eff}) = 0.996727$ and $\mathrm{Im}(n_{eff}) = 1.50103 \times 10^{-6}$, respectively. The same quantities for the mode shown in (e) are $\mathrm{Re}(n_{eff}) = 0.996108$ and $\mathrm{Im}(n_{eff}) = 2.15499 \times 10^{-7}$, respectively. Design parameters for T-1DPC: $d_A = 130$ nm, $d_C = 40$ nm, $d_B = 50$ nm, $r_c = 5$ μm, and $N = 15$.

bandgap, this proposed fiber is capable of showing combined surface plasmon and classical waveguiding phenomena as described in [19].

This phenomenon can be explained using the existence condition of hybrid modes of a hollow core uniaxial MTM cladding fiber described in [45]. In order to excite hybrid modes in the core along with surface plasmon polariton (SPP) modes in the cladding of the fiber, either the ($\mu_r\mu_z > 0$, $\epsilon_r\epsilon_z > 0$ and $\epsilon_r\mu_r < 1$) or ($\mu_r\mu_z < 0$, $\epsilon_r\epsilon_z < 0$ and $\epsilon_r\mu_r > 1$) conditions have to be satisfied. The dielectric based classical fibers can never achieve these conditions. Hence, this combined phenomenon is exclusively for MTM fibers. Here, the subscript "*r*" indicates the direction perpendicular to the plane of the unit cell shown in Fig. 1(a), and subscript "*z*" indicates the direction parallel to the plane of the unit cell shown in Fig. 1(a). In Fig. 4(a), the material dispersion has been shown for $\mu_r\mu_z$, $\epsilon_r\mu_r$ and $\epsilon_r\epsilon_z$ for 930 nm to 1000 nm wavelength range. Here, we have calculated the effective material parameters $(\epsilon_r, \epsilon_z, \mu_r, \mu_z)$ for our cascaded unit cell structure using effective medium approximation [46], [47]. As per material and design parameters, at 960 nm, $\mu_r\mu_z$, $\epsilon_r\epsilon_z$ and $\epsilon_r\mu_r$ are 0.3981, 0.3847, and 0.5515, respectively. This clearly satisfies the first set of aforementioned conditions, thereby, supporting combined SPP and Core modes in the proposed fiber as shown in Fig. 4(b). The second set of conditions is satisfied in our system at longer wavelengths. Fig. 4(c) shows the material dispersion for $\mu_r\mu_z$, $\epsilon_r\mu_r$ and $\epsilon_r\epsilon_z$ from 2100 nm to 2400 nm wavelength range. At 2350 nm, the quantities $\mu_r\mu_z$, $\epsilon_r\epsilon_z$ and $\epsilon_r\mu_r$ are –88.83, –0.1816 and 42.33, respectively. Since these values satisfy the second set of conditions discussed above, the fiber again supports SPP and classical core modes simultaneously, as shown in Fig. 4(d).

To demonstrate the guiding properties of the fiber, we have also calculated the confinement loss for different modes using TMM. First, we assume that the cladding is comprised of non-absorptive materials by setting $\gamma_{mA} = \gamma_{mC} = \gamma_{eB} = 0$. Later on, the effect of material absorption on modal loss characteristics of the fiber will be studied. We can see from Fig. 5(b) that the lowest lossy mode is HE_{11}, and the lowest loss occurs at 1.45 μm. Also, at the wavelength range of 1.2 to 1.4 μm, confinement loss pattern of HE_{11} is similar to that of TM_{01} mode. However, with the increase of wavelength, loss associated with HE_{11} mode starts following the pattern of TE_{01} mode. This is probably due to the fact that the TM component of the mixed mode is the most dominant one at lower wavelength range. However, with the increase of wavelength, the TE component of the mixed mode becomes more dominant.

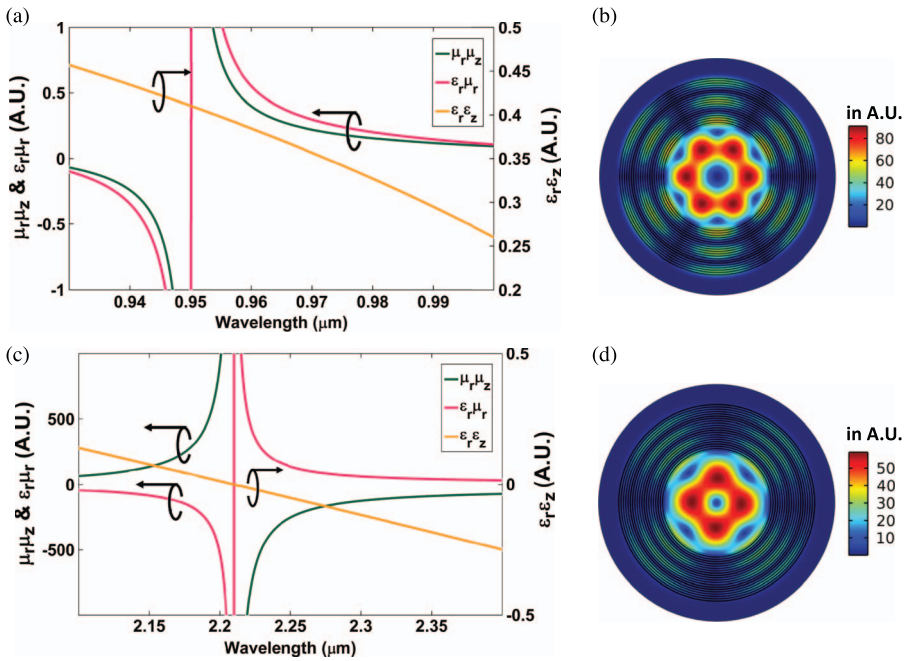

Fig. 4. (a) Dispersion of $\mu_r\mu_z$, $\epsilon_r\mu_r$, and $\epsilon_r\epsilon_z$ from 930 nm to 1000 nm wavelength. (b) Electric field distribution inside the core of the mode with $\mathrm{Re}(n_{eff}) = 0.985583$ and $\mathrm{Im}(n_{eff}) = 1.306083 \times 10^{-7}$ at $\lambda = 960$ nm. (c) Dispersion of $\mu_r\mu_z$, $\epsilon_r\mu_r$, and $\epsilon_r\epsilon_z$ from 2100 nm to 2400 nm wavelength. (d) Electric field distribution inside the core of the mode with $\mathrm{Re}(n_{eff}) = 0.946116$ and $\mathrm{Im}(n_{eff}) = 4.060086 \times 10^{-9}$ at $\lambda = 2350$ nm. The fiber design parameters are $d_A = 130$ nm, $d_C = 40$ nm, $d_B = 50$ nm, $r_c = 5$ μm, and $N = 20$.

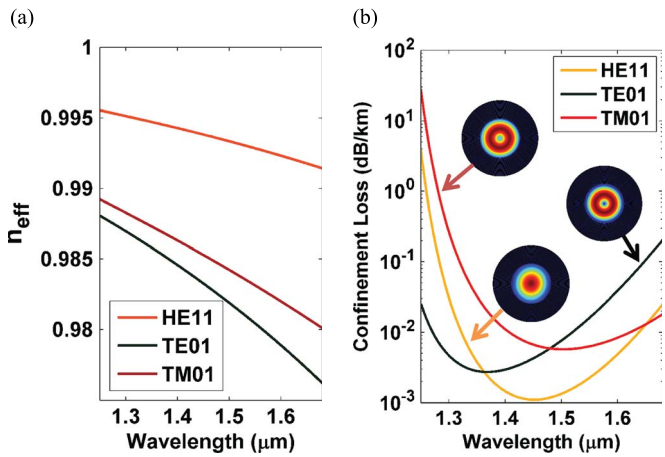

Fig. 5. (a) Effective index. (b) Confinement losses and corresponding electric field distributions for HE_{11}, TE_{01}, and TM_{01}, modes. The fiber design parameters are $d_A = 130$ nm, $d_C = 40$ nm, $d_B = 50$ nm, $r_c = 5$ μm, and $N = 15$.

To compare the waveguiding properties of T-1DPC-based and B-1DPC-based MTM fiber, the loss characteristics of the two structures have been investigated for HE_{11} mode. The material and design parameters used here are the same as that of Fig. 2. For $N = 15$ in both cases, the radiation loss is 3 orders of magnitude lower at 1.55 μm in the T-1DPC-based MTM fiber than that in the B-1DPC-based, as shown in Fig. 6(a). For $N = 15$, T-1DPC-based MTM fiber has more SNG thickness (3300 nm) than that of B-1DPC, which is 2700 nm. One might argue that the reason for the lower loss in T-1DPC-based MTM fiber is the greater SNG thickness. Hence,

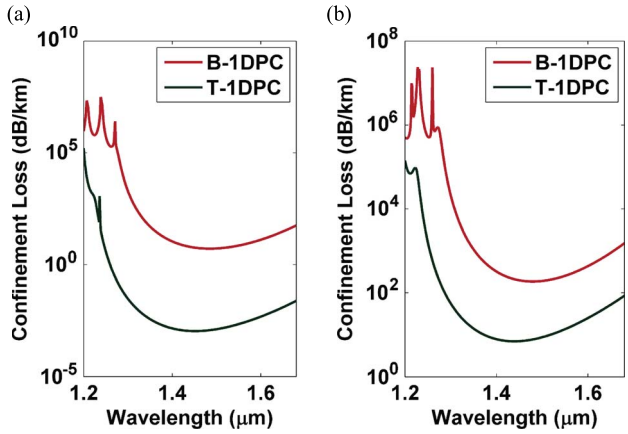

Fig. 6. (a) Comparison of confinement loss for HE_{11} mode in T-1DPC-based and B-1DPC-based MTM bandgap fiber. Here, $N = 15$ for both T-1DPC-based and B-1DPC-based system. (b) Comparison of confinement loss for HE_{11} mode in T-1DPC-based and B-1DPC-based MTM bandgap fiber. Here, $N = 9$ for T-1DPC-based system and $N = 11$ for B-1DPC-based system, making the cladding thickness same (1980 nm) in both cases. The fiber design parameters for T-1DPC are $d_A = 130$ nm, $d_C = 40$ nm, $d_B = 50$ nm, and $r_c = 5$ μm; for B-1DPC, they are $d_A = 130$ nm, $d_B = 50$ nm, and $r_c = 5$ μm.

another simulation is performed to compare the two structures considering the same thickness of the cladding for both T-1DPC and B-1DPC-based system. If $N = 9$ is chosen for T-1DPC and $N = 11$ for B-1DPC, both fibers would have the same cladding thickness of 1980 nm. Again, as Fig. 6(b) shows, the confinement loss in T-1DPC-based fiber is at least 1 order of magnitude lower than that of B-1DPC at 1.55 μm. This can be attributed to the fact that T-1DPC bandgap has higher reflectivity, even with a smaller number of unit cells (N). This indicates that the number of unit cells in the T-1DPC-based MTM fiber may be reduced for the same loss.

From designer's point of view, it is vital to know the effect of physical parameters of the fiber on its guiding properties. For this fiber, the core size and number of unit cell in the cladding are two factors that designers can play with given that materials are fixed. To study the effect of the core size on the confinement loss of the fiber, we varied the core radius from 2 to 10 μm keeping the other parameters same as those used in Fig. 2(b) for the T-1DPC-based MTM fiber. With N fixed at 15, confinement loss at 1.55 μm wavelength is calculated for HE_{11}, TE_{01} and TM_{01} mode as plotted in Fig. 7(a). In this case, the loss decreases with the core radius in $1/r_c^3$ fashion. The loss variance as the core radius varies is similar in manner as Bragg fiber [48]. Moreover, simulation reveals that for T-1DPC-based MTM fiber, at 1.55 μm wavelength, HE_{11} mode achieves the maximum confinement in the hollow core at a relatively lower core radius than TE_{01} and TM_{01} mode as shown in Fig. 7(b). TE_{01} mode has the weakest confinement in the hollow core, and it achieves maximum confinement at a greater core radius than TM_{01} mode. In Fig. 7(c), we also have shown the effect of core radius on dispersion of the fiber. We calculated the dispersion of the fiber for the core radii of 2, 4 and 6 μm. As the core radius increases, dispersion becomes increasingly flat. This can be attributed to the fact that at greater core radius, the confinement is tighter. Hence, the greater core radius shows flat dispersion profile. On a different note, from fabrication perspective, it is always desirable to minimize the number of cladding layers. Therefore, we investigated the effect of number of unit cells in the cladding on confinement loss of the fiber as shown in Fig. 7(d). It turns out that for HE_{11}, TM_{01} and TE_{01} modes, confinement losses are below 0.2 dB/km with cladding comprised of 10, 11, and 12 unit cells, respectively. It is important to note that the silica-based glass fibers exhibit losses about 0.2 dB/km.

From above observations, it is obvious that the TE_{01} mode has the lowest confinement in the core compared to the other modes. This can be explained by a careful investigation into our proposed structure. The layer thicknesses of the proposed T-1DPC unit cell are: $d_A = 130$ nm,

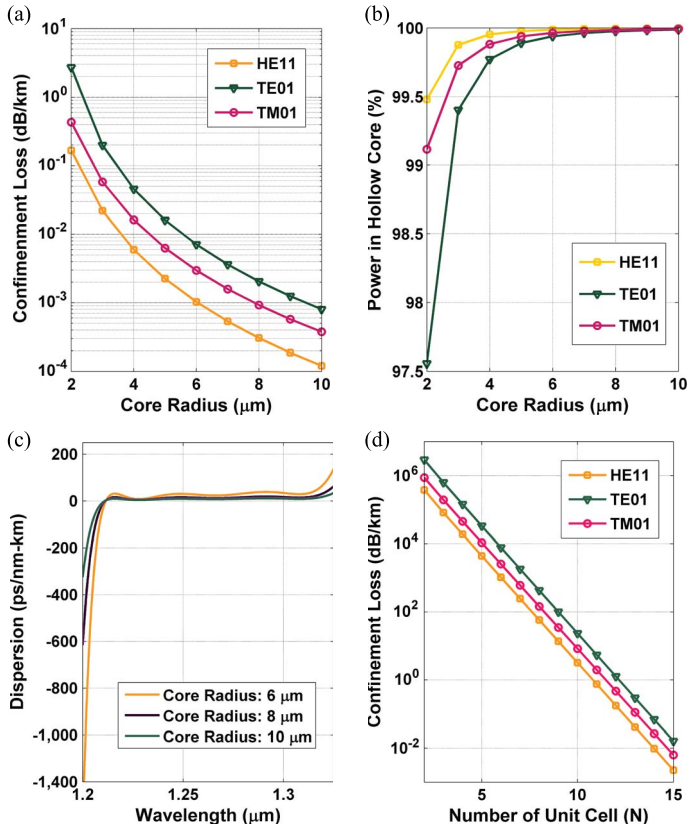

Fig. 7. (a) Confinement loss of HE_{11}, TE_{01}, and TM_{01} mode as a function of core size in T-1DPC-based MTM fiber at 1.55 μm. (b) Percentage of power in the hollow core as a function of core radius for HE_{11}, TE_{01}, and TM_{01} mode at 1.55 μm. (c) Dispersion of the fiber as a function of wavelength for core radii of 6, 8, and 10 μm. (d) Confinement loss at 1.55 μm for HE_{11}, TE_{01}, and TM_{01} mode as a function of N (number of unit cells). In (a)–(c), $N = 15$.

$d_C = 40$ nm, $d_B = 50$ nm. It is important to recall that layer A and layer C of the proposed T-1DPC unit cell are MNG materials while layer B is ENG material. This means, 77% of the cladding material is comprised of MNG material while only 23% of the cladding material is ENG. Since the ENG materials reflect specifically TE light [17] and the percentage of the ENG material in the cladding is relatively low, the TE_{01} mode exhibits the weakest confinement in the core.

As shown earlier, the proposed fiber exhibits sufficiently lower confinement loss than that of silica-based fiber in the communication region. However, the effect of material absorption loss also needs to be taken into account for this MTM fiber. So far, we have demonstrated the guiding property of the fiber assuming the materials are non-absorptive, but now, we investigate the effect of material damping factor on the loss characteristics of our fiber. For simulation, we consider the same structure as used in Fig. 2(b), but we varied the damping factor which contributes to the material loss.

Fig. 8 shows the dependence of loss in the fiber on material damping factor for HE_{11} mode. We have simulated for damping factors $\gamma_{mA} = \gamma_{mC} = \gamma_{eB} = 0, 10^6, 10^9, 10^{12}$ Hz. The result shows strong dependence of fiber loss on material properties. The cladding material absorption loss plays a vital role in the waveguiding. The modal loss increases very rapidly with the increase of material damping factor.

On the other hand, since the cladding of our proposed fiber is structured, structural losses will also be present. However, since the optical wave is getting reflected from the interface of the core and cladding, the structural loss may not play a significant role in this type of fiber.

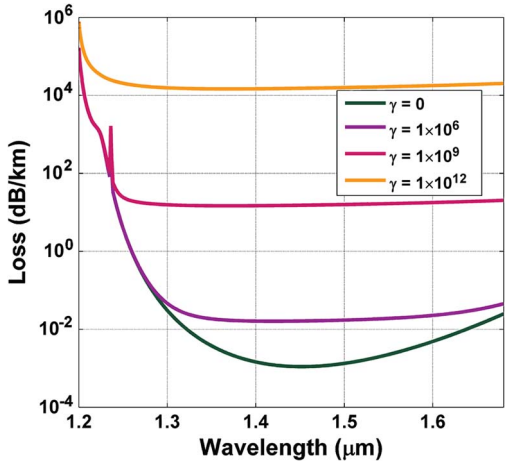

Fig. 8. Total loss of HE_{11} mode in 1.2 to 1.8 μm window for damping factors $\gamma_{mA} = \gamma_{mC} = \gamma_{eB} = 0, 10^6, 10^9$, and 10^{12} Hz.

4. Conclusion and Future Work

A single negative T-1DPC-based MTM cladding fiber is demonstrated as a robust architecture for achieving broadband transmission. The cladding of the fiber is made of a series of unit cells consisting of different Mu and epsilon negative materials. By employing TMM and FE methods, we numerically investigate the PBG and modal loss characteristics of the fiber. The T-1DPC-based MTM cladding can effectively broaden the PBG. For most of the PBG range, the confinement loss of the T-1DPC-based MTM fiber can be significantly reduced compared with that of the B-1DPC-based fiber. The lower loss in the fiber is essentially due to the higher reflectivity obtained in the T-1DPC-based cladding than that in the B-1DPC-based. We have also shown that the fiber is capable of demonstrating simultaneous classical core wave guidance and surface plasmon propagation. This property of the fiber may pave way to ultra-fast communication and biosensing. From the study of material absorption in fiber, it can be concluded that future fabrication techniques should address the material absorption issue in order to make the fiber practical for real world application. However, as metamaterials are artificially engineered materials, it is possible to tune the damping factor to such value that the cladding absorption loss does not play a significant role. We believe, this type of fiber can be physically realized using the fiber drawing technique described in [20] and [21] in a pixelated ring Bragg fiber [49].

Acknowledgment

The authors would like to thank U. Hanif and W. L. Ng for their help.

References

[1] U. Leonhardt, "Optical conformal mapping," *Science*, vol. 312, no. 5781, pp. 1777–1780, Jun. 2006. [Online]. Available: http://www.sciencemag.org/content/312/5781/1777
[2] J. B. Pendry, "Negative refraction makes a perfect lens," *Phys. Rev. Lett.*, vol. 85, no. 18, pp. 3966–3969, Oct. 2000. [Online]. Available: http://link.aps.org/doi/10.1103/PhysRevLett.85.3966
[3] J. B. Pendry, D. Schurig, and D. R. Smith, "Controlling electromagnetic fields," *Science*, vol. 312, no. 5781, pp. 1780–1782, Jun. 2006. [Online]. Available: http://www.sciencemag.org/content/312/5781/1780
[4] D. R. Smith, W. J. Padilla, D. C. Vier, S. C. Nemat-Nasser, and S. Schultz, "Composite medium with simultaneously negative permeability and permittivity," *Phys. Rev. Lett.*, vol. 84, no. 1, pp. 4184–4187, May 2000. [Online]. Available: http://link.aps.org/doi/10.1103/PhysRevLett.84.4184
[5] Y.-R. Li, R.-M. Ho, and Y.-C. Hung, "Plasmon hybridization and dipolar interaction on the resonances of helix metamaterials," *IEEE J. Photon.*, vol. 5, no. 2, Apr. 2013, Art. ID 2700510.
[6] W. Withayachumnankul and D. Abbott, "Metamaterials in the terahertz regime," *IEEE J. Photon.*, vol. 1, no. 2, pp. 99–118, Aug. 2009.

[7] Z. Lu, W. Zhao, and K. Shi, "Ultracompact electroabsorption modulators based on tunable epsilon-near-zero-slot waveguides," *IEEE J. Photon.*, vol. 4, no. 3, pp. 735–740, Jun. 2012.

[8] W. Zhu, I. D. Rukhlenko, and M. Premaratne, "Maneuvering propagation of surface plasmon polaritons using complementary medium inserts," *IEEE J. Photon.*, vol. 4, no. 3, pp. 741–747, Jun. 2012.

[9] R. Ruppin, "Surface polaritons and extinction properties of a left-handed material cylinder," *J. Phys. Condens. Matter*, vol. 16, no. 34, pp. 5991–5998, Aug. 2004.

[10] H. Cory and T. Blum, "Surface-wave propagation along a metamaterial cylindrical guide," *Microw. Opt. Technol. Lett.*, vol. 44, no. 1, pp. 31–35, Jan. 2005.

[11] A. V. Novitsky and L. Barkovsky, "Guided modes in negative-refractive-index fibres," *J. Opt. A, Pure Appl. Opt.*, vol. 7, no. 2, pp. S51–S56, Jan. 2005.

[12] A. V. Novitsky, "Negative-refractive-index fibres: TEM modes," *J. Opt. A, Pure Appl. Opt.*, vol. 8, no. 10, pp. 864–866, Oct. 2006.

[13] L. Shen and Z. Wang, "Guided modes characteristics in a fiber with left-handed material," *Microw. Opt. Technol. Lett.*, vol. 49, no. 5, pp. 1039–1041, May 2007.

[14] L. F. Shen and Z. H. Wang, "Guided modes in fiber with left-handed materials," *J. Opt. Soc. Amer. A, Opt. Image Sci.*, vol. 26, no. 4, pp. 754–759, Apr. 2009.

[15] K. Y. Kim, J.-H. Lee, Y. Cho, and H.-S. Tae, "Electromagnetic wave propagation through doubly dispersive subwavelength metamaterial hole," *Opt. Exp.*, vol. 13, no. 10, pp. 3653–3665, May 2005.

[16] K. Y. Kim, "Fundamental guided electromagnetic dispersion characteristics in lossless dispersive metamaterial clad circular air-hole waveguides," *J. Opt. A, Pure Appl. Opt.*, vol. 9, no. 11, pp. 1062–1069, Nov. 2007.

[17] M. Yan and N. A. Mortensen, "Hollow-core infrared fiber incorporating metal-wire metamaterial," *Opt. Exp.*, vol. 17, no. 17, pp. 14851–14864, Aug. 2009.

[18] S. Schwaiger *et al.,* "Rolled-up three-dimensional metamaterials with a tunable plasma frequency in the visible regime," *Phys. Rev. Lett.*, vol. 102, no. 16, Apr. 2009, Art. ID 163903.

[19] E. J. Smith, Z. Liu, Y. Mei, and O. G. Schmidt, "Combined surface plasmon and classical waveguiding through metamaterial fiber design," *Nano Lett.*, vol. 10, no. 1, pp. 1–5, Jan. 2009.

[20] A. Tuniz *et al.,* "Drawn metamaterials with plasmonic response at terahertz frequencies," *Appl. Phys. Lett.*, vol. 96, no. 19, May 2010, Art. ID 191101.

[21] A. Tuniz *et al.,* "Stacked-and-drawn metamaterials with magnetic resonances in the terahertz range," *Opt. Exp.*, vol. 19, no. 17, pp. 16480–16490, Aug. 2011.

[22] J. Pendry, A. Holden, W. Stewart, and I. Youngs, "Extremely low frequency plasmons in metallic mesostructures," *Phys. Rev. Lett.*, vol. 76, no. 25, pp. 4773–4776, Jun. 1996.

[23] Y. Xiang, X. Dai, S. Wen, Z. Tang, and D. Fan, "Zero-effective-phase bandgaps in photonic multilayers: Analytic expressions for band-edge frequencies and broadband omnidirectional reflection," *J. Opt. Soc. Amer. B, Opt. Phys.*, vol. 28, no. 5, pp. 1187–1193, May 2011.

[24] H. Jiang *et al.,* "Properties of one-dimensional photonic crystals containing single-negative materials," *Phys. Rev. E, Stat. Nonlinear Soft Matter Phys.*, vol. 69, no. 6, Jun. 2004, Art. ID 066607.

[25] Y. Weng, Z.-G. Wang, and H. Chen, "Band structures of one-dimensional subwavelength photonic crystals containing metamaterials," *Phys. Rev. E, Stat. Nonlinear Soft Matter Phys.*, vol. 75, no. 4, Apr. 2007, Art. ID 046601.

[26] M. J. Shawon *et al.,* "Quantum mechanical equivalent of electromagnetic band gap and perfect tunneling in multilayer semiconductor hetero-structures," in *Proc. IEEE ICECE*, 2014, pp. 196–199.

[27] T. Wang, J. Dong, C. Yin, and H. Wang, "Complete evanescent tunneling gaps in one-dimensional photonic crystals," *Phys. Lett. A*, vol. 373, no. 1, pp. 169–172, Dec. 2008.

[28] L.-G. Wang, H. Chen, and S.-Y. Zhu, "Omnidirectional gap and defect mode of one-dimensional photonic crystals with single-negative materials," *Phys. Rev. B, Condens. Matter Mater. Phys.*, vol. 70, no. 24, Dec. 2004, Art. ID 245102.

[29] Y. Xiang, X. Dai, S. Wen, Z. Tang, and D. Fan, "Extending the zero-effective-phase photonic bandgap by one-dimensional ternary photonic crystals," *Appl. Phys. B*, vol. 103, no. 4, pp. 897–906, Jun. 2011.

[30] A. Shahriar, M. Mahdy, J. Shawon, G. D. Al-Quaderi, and M. Matin, "On the relation between perfect tunneling and band gaps for SNG metamaterial structures," *arXiv preprint arXiv:1308.3260*, 2013.

[31] M. M. Hasan, D. S. Kumar, M. R. C. Mahdy, D. N. Hasan, and M. A. Matin, "Robust optical fiber using single negative metamaterial cladding," *IEEE Photon. Technol. Lett.*, vol. 25, no. 11, pp. 1043–1046, Jun. 2013.

[32] T. Fujishige, C. Caloz, and T. Itoh, "Experimental demonstration of transparency in the ENG-MNG pair in a CRLH transmission-line implementation," *Microw. Opt. Technol. Lett.*, vol. 46, no. 5, pp. 476–481, Sep. 2005.

[33] L. Zhang, Y. Zhang, L. He, H. Li, and H. Chen, "Experimental study of photonic crystals consisting of ϵ-negative and μ-negative materials," *Phys. Rev. E, Stat. Nonlinear Soft Matter Phys.*, vol. 74, no. 5, Nov. 2006, Art. ID 056615.

[34] Y. Chen, "Broadband one-dimensional photonic crystal wave plate containing single-negative materials," *Opt. Exp.*, vol. 18, no. 19, pp. 19920–19929, Sep. 2010.

[35] Y. Chen, "Defect modes merging in one-dimensional photonic crystals with multiple single-negative material defects," *Appl. Phys. Lett.*, vol. 92, no. 1, Jan. 2008, Art. ID 011925.

[36] L.-G. Wang, N.-H. Liu, Q. Lin, and S.-Y. Zhu, "Propagation of coherent and partially coherent pulses through one-dimensional photonic crystals," *Phys. Rev. E, Stat. Nonlinear Soft Matter Phys.*, vol. 70, no. 1, Jul. 2004, Art. ID 016601.

[37] D.-W. Yeh and C.-J. Wu, "Analysis of photonic band structure in a one-dimensional photonic crystal containing single-negative materials," *Opt. Exp.*, vol. 17, no. 19, pp. 16666–16680, Sep. 2009.

[38] N. W. Ashcroft and N. D. Mermin, *Solid State Physics*, 1st ed. Philadelphia, PA, USA: Harcourt, 1976, pp. 1–20.

[39] P. Yeh, *Optical Waves in Layered Media*, vol. 95. New York, NY, USA: Wiley, 1988.

[40] A. Argyros, "Guided modes and loss in Bragg fibres," *Opt. Exp.*, vol. 10, no. 24, pp. 1411–1417, Dec. 2002. [Online]. Available: http://www.opticsexpress.org/abstract.cfm?URI=oe-10-24-1411

[41] P. Yeh, A. Yariv, and E. Marom, "Theory of Bragg fiber," *J. Opt. Soc. Amer.*, vol. 68, no. 9, pp. 1196–1201, Sep. 1978.

[42] S. Guo, S. Albin, and R. Rogowski, "Comparative analysis of Bragg fibers," *Opt. Exp.*, vol. 12, no. 1, pp. 198–207, Jan. 2004.
[43] L. Shang, X. Yang, Y. Xia, and H. Wang, "Hollow core Bragg fibers with a heterostructured cladding based on ternary one-dimensional photonic crystal for mid-infrared broadband and low-loss transmission," *J. Lightw. Technol.*, vol. 32, no. 9, pp. 1717–1725, May 2014.
[44] D. J. J. Hu, G. Alagappan, Y.-K. Yeo, P. P. Shum, and P. Wu, "Broadband transmission in hollow-core Bragg fibers with geometrically distributed multilayered cladding," *Opt. Exp.*, vol. 18, no. 18, pp. 18671–18684, Aug. 2010.
[45] S. Atakaramians, A. Argyros, S. C. Fleming, and B. T. Kuhlmey, "Hollow-core waveguides with uniaxial metamaterial cladding: Modal equations and guidance conditions," *J. Opt. Soc. Amer. B, Opt. Phys.*, vol. 29, no. 9, pp. 2462–2477, Sep. 2012.
[46] B. Wood, J. B. Pendry, and D. P. Tsai, "Directed subwavelength imaging using a layered metal-dielectric system," *Phys. Rev. B, Condens. Matter Mater. Phys.*, vol. 74, no. 11, Sep. 2006, Art. ID 115116. [Online]. Available: http://link.aps.org/doi/10.1103/PhysRevB.74.115116
[47] Z.-G. Dong, S.-N. Zhu, and H. Liu, "Numerical simulations of negative-index refraction in a lamellar composite with alternating single negative layers," *Chin. Phys.*, vol. 15, no. 8, pp. 1772–1776, Aug. 2006.
[48] Y. Xu, A. Yariv, J. Fleming, and S.-Y. Lin, "Asymptotic analysis of silicon based Bragg fibers," *Opt. Exp.*, vol. 11, no. 9, pp. 1039–1049, May 2003. [Online]. Available: http://www.opticsexpress.org/abstract.cfm?URI=oe-11-9-1039
[49] A. Baz, G. Bouwmans, L. Bigot, and Y. Quiquempois, "Pixelated high-index ring Bragg fibers," *Opt. Exp.*, vol. 20, no. 17, pp. 18795–18802, Aug. 2012. [Online]. Available: http://www.opticsexpress.org/abstract.cfm?URI=oe-20-17-18795